3D-Imaging of synapses in neuronal tissues with synchrotron X-ray ptychography

Carles Bosch[1], Ana Diaz[3], Mirko Holler[3], Manuel Guizar-Sicairos[3,6], Tomas Aidukas[3], Alexandra Pacureanu[4], Elisabeth Müller[3], Christopher J. Peddie[5], Lucy Collinson[5], Yuxin Zhang[1,2], Andreas Menzel[3], Adrian A. Wanner*[3], Andreas T. Schaefer*[1,2]

1 Sensory Circuits and Neurotechnology Lab, The Francis Crick Institute, London, UK.
2 Department of Neuroscience, Physiology and Pharmacology, University College, London, UK.
3 Paul Scherrer Institute, Villigen, Switzerland.
4 ESRF, The European Synchrotron, Grenoble, France.
5 Electron Microscopy STP, The Francis Crick Institute, London, UK.
6 Institute of Physics, École Polytechnique Fédérale de Lausanne, Lausanne, CH.
* correspondence: adrian.wanner@psi.ch; andreas.schaefer@crick.ac.uk

Abstract:
Wiring diagrams of neural circuits are of central importance in delineating mechanisms of computation in the brain (Lichtman and Sanes, 2008; Litwin-Kumar and Turaga, 2019). To generate these diagrams, the individual parts of neurons - axons, dendrites and synapses - must be densely identified in 3-dimensional volumes of neuronal tissue. This is typically achieved by electron microscopy (Kornfeld and Denk, 2018), necessitating physical sectioning of the specimen either before or during the image acquisition process using ultrathin sectioning techniques or gallium or gas cluster ion beams (Denk and Horstmann, 2004; Hayworth et al., 2020; Kasthuri et al., 2015; Xu et al., 2017). Here, we demonstrate that X-ray ptychography (Pfeiffer, 2018), a coherent diffractive X-ray imaging technique, can faithfully acquire 3-dimensional images of metal-stained mouse neuronal tissue. Achieving high imaging quality requires minimization of the radiation damage to the sample, which we achieve by imaging at cryogenic temperatures and using specialised tomographic reconstruction algorithms (Odstrcil et al., 2019b). Using a newly identified tri-functional epoxy resin we demonstrate radiation resistance to X-ray doses exceeding 10^{11} Gy. Sub-40 nm resolution makes it possible to densely resolve axon bundles, boutons, dendrites, and synapses without physical sectioning. Moreover, the tissue volumes can subsequently be imaged in 3D using high-resolution focused ion beam scanning electron microscopy (FIB-SEM) (Heymann et al., 2006; Knott et al., 2008) showing intact ultrastructure, suggesting that metal-stained neuronal tissue can be highly radiation-stable. Ongoing improvements in synchrotron, X-ray and detector physics (Yabashi and Tanaka, 2017), as well as further optimization of sample preparation and staining procedures (Hua et al., 2015; Karlupia et al., 2023; Lu et al., 2023; Mikula and Denk, 2015; Pallotto et al., 2015; Song et al., 2022), could lead to substantial improvements in acquisition speed (Du et al., 2021), whilst widening the volumes that can be imaged with X-ray techniques using laminography (Helfen et al., 2005; Helfen et al., 2013; Holler et al., 2020b; Holler et al., 2019) and nano-holotomography (Cloetens et al., 1999; Kuan et al., 2020) could allow for non-destructive X-ray imaging of synapses and neural circuits contained in volumes of increasing size.

Introduction:

Determining the connectome, the wiring diagram of a brain region or possibly an entire brain, promises to deliver similar benefits to neuroscience as determining genomes has brought to biology (Abbott et al., 2020; Lichtman and Sanes, 2008). In particular, the connectome will provide blueprints onto which other data, such as physiological, biochemical or genetic information, can be mapped and compared between species, conditions or developmental stages to constrain models of circuit function (Litwin-Kumar and Turaga, 2019). To map the connectome, a diverse toolbox of reliable, efficient methods needs to be employed in combination with a variety of other approaches. Crucially, they must be capable of resolving the fine structures of axons, dendrites and synapses.

While superresolution optical imaging techniques hold promise for detailed analysis of stained samples (Gao et al., 2019; Huang et al., 2009; Igarashi et al., 2018; Tonnesen et al., 2018), current gold-standard methods for dense tissue reconstruction rely on electron microscopy (Bock et al., 2011; Briggman and Bock, 2012; Hayworth et al., 2014; Helmstaedter, 2013; Horstmann et al., 2012; Klinger et al., 2021; Kornfeld and Denk, 2018; Phelps et al., 2021). As electron penetration depth into tissue is limited to a few nm (Du and Jacobsen, 2018; Henderson, 1995), obtaining 3-dimensional information requires tissue sectioning or milling either before preparing samples for imaging (Bock *et al.*, 2011; Hayworth *et al.*, 2014; Horstmann *et al.*, 2012) or during image acquisition (Denk and Horstmann, 2004; Hayworth *et al.*, 2020; Xu *et al.*, 2017). These workflows present significant challenges for reliable continuous image acquisition, with the risk of information loss during month-long experiments, and experimental analysis which requires reconstruction and alignment of multimodal datasets.

X-rays have the ability to penetrate samples of several mm to cm making it possible to perform largely non-destructive imaging of tissues (Du and Jacobsen, 2018; Henderson, 1995) using a broad range of tools and methods. Laboratory X-ray sources have recently been shown to be capable of resolving cell bodies and even large neurites (Topperwien et al., 2018); however, the limited radiation flux makes imaging of large samples extremely time-consuming. Large-scale synchrotron facilities can provide high-flux coherent X-rays at wavelengths in the Ångstrom range, thereby making it possible to image larger samples at higher resolutions, driving the development of imaging methods capable of providing 3D resolution down to 10s of nanometers for hard, inorganic nanostructures with high-density contrast (Grishina et al., 2019; Holler et al., 2017a; Holler *et al.*, 2019; Michelson et al., 2022). Application of these methods to biological imaging has enabled reliable identification of various biological features including blood vessels, cell bodies and large neurites (Bosch et al., 2022; Cedola et al., 2017; Dyer et al., 2017; Fonseca et al., 2018; Khimchenko et al., 2018; Mizutani et al., 2013; Momose et al., 1996; Panneels et al., 2021; Reichardt et al., 2021; Schulz et al., 2010; Shahmoradian et al., 2017; Walsh et al., 2021). More recently, thin neurites were identified at a resolution of ~100 nm using nano-holotomography (Kuan *et al.*, 2020). Fundamentally however, the resolution in X-ray tomography scales with the 4th power of the radiation dose i.e. to increase the resolution by a factor of 5 in the same sample, the X-ray dose needs to be increased by 5^4=625x. X-ray imaging of soft biological tissue was previously thought to be limited by tissue contrast and by the radiation dose that can be employed before the tissue is damaged (Du and Jacobsen, 2018; Henderson, 1995; Howells et al., 2009), and it remained unclear whether key ultrastructural features such as synapses could in principle be resolved with X-rays.

To overcome the poor X-ray image contrast inherent to soft tissues, we combine heavy-metal staining protocols developed for volume electron microscopy (Hua *et al.*, 2015) with high-resolution ptychographic tomography (Holler *et al.*, 2017a; Holler et al., 2012). Radiation damage is minimised by imaging samples under cryogenic conditions using a recently developed cryogenic ptychographic tomography instrument (Holler et al., 2018; Shahmoradian *et al.*, 2017) and by embedding in a newly identified highly radiation-resistant resin (Van De Voorde, 1970; Wu et al., 2011). Residual sample deformations will introduce inconsistencies between the acquired projections, for which we compensate computationally in order to avoid loss of 3D reconstruction quality (Odstrcil *et al.*, 2019b). By combining these techniques, we obtain an isotropic 3D resolution of 38 nm for neural tissue, sufficient for resolving synapses, while simultaneously maintaining tissue integrity.

Results

X-ray ptychography is performed by scanning a sample across a confined, coherent beam a few µm in diameter and measuring diffraction patterns in the far field (Fig 1a)(Pfeiffer, 2018). Using iterative reconstruction algorithms (Guizar-Sicairos et al., 2014; Rodenburg and Maiden, 2019), these diffraction patterns (Fig 1a) are then used to reconstruct phase images, which are proportional to the projected electron density of the sample (Fig 1b). To perform ptychographic X-ray computed tomography (PXCT), the projections are acquired at multiple sample rotation angles from 0 to 180 degrees, followed by tomographic reconstruction of a 3D sample volume (Fig 1c). Resolution in X-ray ptychography is limited not by the spot size but by the angular acceptance angle of the detector (which determines the maximum observable spatial frequencies) and the applied X-ray dose (which determines the signal-to-noise ratio of the spatial frequencies within the recorded diffraction patterns). Since imaging geometry can be adjusted relatively easily, radiation damage and weak intrinsic scattering of biological tissues are the main factors limiting the attainable resolution (Du *et al.*, 2021; Henderson, 1995; Howells *et al.*, 2009). We therefore employed a recently developed cryo-tomography stage (Holler *et al.*, 2018) to cool samples to <95 K and reduce the structural changes caused by such damage, in combination with a staining and embedding protocol to maximise contrast. Additionally, we applied a new non-rigid tomography reconstruction algorithm, designed to compensate for radiation-induced deformation of the sample (Odstrcil *et al.*, 2019b). In the following, we present tomograms from mouse brain tissue (the radiatum layer of hippocampus, the external plexiform and glomerular layers from the olfactory bulb, and upper layers of neocortex as structures rich in neurites and dendritic shaft and spine synapses) at different radiation doses. Given the limited experimental time, we had to image pillars 10-30 µm in diameter, which were prepared using a focused gallium beam.

In a sample of external plexiform layer tissue from mouse olfactory bulb, at a dose of 1.8×10^7 Gy we were already able to resolve dendrites in a 2D reslice (Fig 2(a1)). Using Fourier shell correlation (FSC, Fig 2(c))(Harauz and van Heel, 1986; van Heel and Schatz, 2005) we estimated an isotropic 3D resolution of 84 nm (Fig 2(f)). Cryo-cooling is thought to reduce structural changes that limit resolution in X-ray imaging due to radiation damage (Beetz and Jacobsen, 2003; Henderson, 1995). Consistent with that notion, tomograms acquired at this radiation dose did not show any indication of significant blurring or other signs of structural changes due to radiation damage. Increasing dose to 8.4×10^7 Gy improved 3D resolution to 69 nm (Fig 2(a2, d, f)). However, contrary to theoretical

expectations (Du *et al.*, 2021), at even higher doses of $3.8x10^8$ Gy resolution did not further improve (70 nm; Fig 2(a3, e, f)). In particular, we noted that the sample deformed, presumably due to "softening" of the embedding resin, as seen when comparing projections from the same angle (but acquired with ~$2.6x10^8$ Gy intermittent irradiation, Supp Fig 2.1). As a result, the resolution of the tomogram decreased (Fig 2(a3, e)) based on visual blurring in the 3D volume and the loss of spatial frequencies based on FSC analysis (Fig 2(e)). To take these sample changes into account we applied a non-rigid tomography reconstruction approach that estimates the deformations between the projections and includes them in the tomographic reconstruction (Odstrcil *et al.*, 2019b). This deformation correction method requires specialized data acquisition where the whole angular range from 0 to 180 degrees is split into multiple equally spaced angular ranges to acquire multiple subtomograms. In doing so, each subtomogram provides a low-resolution snapshot of the sample at a given time point. By calculating the 3D optical flow between these subtomograms the deformation fields can be estimated across a range of time points and interpolated to describe the changes between all of the collected projections. Accounting for radiation-induced changes in this manner not only recovered lower spatial frequencies (as seen in Fig 2(b) and from FSC in Fig 2(c-e), Supp Fig 2.1) but further improved 3D resolution to 49.7 nm (Fig 2(f)), ie, close to the theoretical predictions. The use of non-rigid tomography consistently preserved the expected scaling between the radiation dose and attainable resolution across the measured samples (Supp Fig 2.2). Measured at a temperature of ~90 K, Epon-embedded tissue was radiation-stable at doses up to $6x10^8$ Gy (Supp Fig 2.3).

With this improved approach we obtained 3D tomograms from a variety of brain regions, including olfactory bulb external plexiform layer, glomerular layer, hippocampus stratum radiatum, and layer 2 of somatosensory cortex (Fig 3). This allowed us to visualise e.g. neurites (Fig 3, green), mitochondria (Fig 3, red), myelin (Fig 3, black), or nuclei (Fig 3, light blue).

A decisive feature for connectomics is the detection of synaptic contacts (Fig 4). Thus, we assessed whether PXCT would allow the identification of such structures. Indeed, at the highest resolution image we acquired, structures resembling synapses became apparent (Fig 4(b)). As PXCT (Fig 4(a, left)) is a largely non-destructive technique we could subsequently process the same specimen using focused ion beam milling combined with scanning electron microscopy (FIB-SEM, Fig 4(a, right)). This allowed us to obtain insight into potential ultrastructural alterations induced by the X-ray irradiation as well as obtain "ground truth" for structure identification and further quantification. The FIB-SEM reconstruction showed a mild curtaining effect that might be the consequence of radiation-induced changing to the embedding medium (Supp Fig 4.1). However, overall ultrastructure was not noticeably impacted by prior X-ray radiation dosage of ~$4x10^8$ Gy (Fig 4(c)). In particular, membranes were left intact as were subcellular features such as mitochondria, endoplasmic reticulum or dendritic membranes (Fig 4(c) and Supp Fig 4.1f). Aligning the FIB-SEM with the PXCT dataset allowed us to directly compare structures identified in PXCT with ground truth data obtained from FIB-SEM (Fig 4(b,c)). Indeed, structures identified as synapses in PXCT were readily recognisable as such in the FIB-SEM dataset (Fig 4(b,c), center). To quantify the reliability of synapse identification, we performed two approaches: Firstly, we traced individual dendrites in both datasets (Fig 4(d)) and manually labelled synapses independently in both datasets (Fig 4(d)). More than two-thirds of synapses identified in the SEM dataset were recognized in the blind analysis of PXCT images (225/338 synapses, 70±6%, n=5 dendrites Fig 4(d)). Additionally, to obtain true estimates of precision

and reliability, three annotators were presented with randomly located browsable 1 μm^3 volumes of the FIB-SEM or PXCT datasets (Supp Fig 4.2). Annotators were asked to indicate whether in the volume a synapse was present or not and indicate confidence. Using the FIB-SEM dataset as ground truth again, PXCT annotation showed a recall of synapse presence of 60% with a precision of 80% (Fig 4(e), Supp Fig 4.2).

Increasing resolution further would benefit in particular automated reconstruction methods (Januszewski et al., 2018; Schmidt et al., 2022). However, doing so with X-ray ptychography requires increased X-ray dose. Epon-embedded samples started displaying deformations consistent with mass loss possibly compromising ultrastructural features (Supp Fig. 2.3). In agreement with previous work (Du *et al.*, 2021; Howells *et al.*, 2009), deformations were consistently observed at doses exceeding $6x10^8$ Gy (Supp Fig 2.3). In order to improve radiation resistance we turned to resins previously developed for nuclear reactors or the aerospace industry (Van De Voorde, 1970; Wu *et al.*, 2011) where stability in the presence of ionising radiation is of paramount importance. Screening a battery of such resins, we identified a low-viscosity epoxy with good infiltration properties consisting of triglycidyl para-aminophenol (TGPAP) (Fig 5(a)), a triglycidyl ether of para-aminophenol. TGPAP is a tri-functional epoxy resin, i.e. it contains three epoxy groups per molecule. For curing we used the 4,4'-diaminodiphenyl methane (DDM), a well-known hardener with two primary amine groups that react with the epoxy groups of TGPAP. The presence of three epoxy groups per molecule allows for increased crosslinking density during curing, leading to superior mechanical strength, chemical and radiation resistance, as well as thermal stability. We term this tri-functional epoxy resin "TF (Tough) Resin" (TF). To assess radiation resistance, we exposed samples embedded in Epon or TF to the high X-ray flux from the high brilliance source at ESRF. While Epon samples disintegrated at $<10^9$ Gy, TF samples showed little sign of mass loss or compromise of cellular features even with prolonged exposure (estimated to exceed 10^{11} Gy). Importantly, TF tissue penetration is comparable to commonly used Epon and preserves ultrastructure as verified by FIB-SEM analysis (Fig 5(c)).

Embedding heavy metal-stained tissue in TF therefore allowed us to significantly increase the cumulative radiation dose for PXCT. This in turn enabled us to further increase the resolution that can be achieved with PXCT to 38 nm (Fig 5(b). The resulting resolution was not only sufficient to resolve and segment vesicle clusters, synaptic densities and thin dendritic spine necks (Fig 5(d), Supp Video 5.1, 5.2). Importantly, FIB-SEM milling confirmed that the ultrastructure was intact after irradiation with a dose exceeding 10^{10} Gy. Together, this indicates that using newly identified radiation-resistant embedding materials with heavy metal staining and non-rigid tomographic reconstruction methods, coherent X-ray imaging can provide sufficient resolving power in 3D to identify key connectomic features.

Discussion

Here, we have demonstrated the potential for coherent synchrotron X-ray tomography to image at resolutions sufficient to detect key connectomics features such as synaptic contacts. While employing sub-nm wavelengths, resolution in coherent x-ray imaging of biological soft tissue is generally limited by contrast. Furthermore, the softness of the embedding materials makes it susceptible to radiation damage, which ultimately limits the maximum attainable resolution (Du *et al.*, 2021; Du and Jacobsen, 2018; Henderson, 1995; Howells *et al.*, 2009). When e.g. heavy metal stains are employed, they increase contrast and X-ray absorption, which, however, also acts as a mediator for radiation damage (Du and Jacobsen, 2018; Henderson, 1995; Howells *et al.*, 2009). We employed the tomography

nano cryo stage (OMNY), an instrument that uses an interferometer-guided stage in cryogenic conditions which is optimized for PXCT measurements (Holler *et al.*, 2018). Moreover, we identified an epoxy resin from the nuclear reactor and aerospace industry (Van De Voorde, 1970; Wu *et al.*, 2011) with superior radiation resistance. Together this allowed us to significantly improve the resolution of X-ray imaging of biological tissue to the extent that key structures such as vesicles, synaptic densities or spine necks can be densely detected in 3D.

At a dosage of $4x10^8$ Gy we could see some radiation-induced change, e.g. sample expansion, and some changes such a curtaining effects and small deformations were visible outside the imaged area in the downstream FIB-SEM analysis (Supp Fig 2.1, 4.1). However, none of these alterations resulted in any significant changes to the ultrastructure. e have also shown that adjusting tomography reconstruction algorithms (Odstrcil *et al.*, 2019b) can largely compensate for radiation-induced changes and improve resolution by modelling the tissue expansion explicitly (Fig 2, Supp Fig 2.1). Moreover, the OMNY stage, which we have developed, allows for cooling to liquid He temperatures. It is tempting to speculate that further cooling might further reduce irradiation damage, allowing for further increases in radiation dose and possibly generating higher resolution data output. Importantly, embedding and staining protocols have played a key role in the development and improvement of volume EM techniques (Hua *et al.*, 2015; Mikula and Denk, 2015; Pallotto *et al.*, 2015; Zhang et al., 2022). Epon embedding provides excellent mechanical properties for thin serial sectioning. It is, however, prone to radiation damage (Zimmermann et al., 2022) (Supp Fig 2.3). To enhance radiation resilience we therefore turned to the aerospace and nuclear industry that critically depends on epoxies resistant to ionising radiation. We identified one resin ("TF-resin") that penetrated tissue well, preserving ultrastructure, and showed significantly improved radiation resistance. In fact, we could not observe mass loss or significant damage to tissue samples at radiation exceeding 10^{11} Gy. Theoretical estimates for flux and dose constraints for tomographic imaging indicate that such dose resistance will suffice for whole-mouse brain X-ray tomographic imaging at sub 20 nm resolution (Du *et al.*, 2021).

While not resulting in mass loss or ultrastructural damage, irradiation results in deformations, likely due to thermal expansion or limited impact on chemical bonds and e.g. local gas formation (Supp Fig 2.1). While ultrastructure (e.g. membranes, protein clusters) seems to be largely unimpacted (Figs 4(c) and 5(c)), such deformations result in blurred tomographic reconstructions and consequently limit resolution (Fig 2, Supp Fig 2.1). We therefore employed non-rigid reconstruction methods that partially mitigate these limitations. Improvements of such algorithms or e.g. tomographic acquisition with intermediate, low-dose reference tomograms, might further improve resolution to levels below 10 nm. Correlative volume EM datasets (such as those shown in Figs 4(c) and 5(c)) can provide ground truth for such algorithm development. While providing good contrast, heavy-metal stains might in fact not be ideal for X-ray imaging and materials with similar dissipation butsignificantly reduced absorption (Busse et al., 2021; Reichmann et al., 2023) might further improve sample stability.

One challenge of using PXCT for neural circuit imaging is that the number of projections scales linearly with the imaging resolution and sample diameter. Given limited experimental time, the increase of resolving power inevitably leads to a reduction of the sample volume that can be imaged. This could be circumvented by changing the imaging geometry and employing laminography (Helfen *et al.*, 2005; Helfen *et al.*, 2013; Holler *et al.*, 2020b; Holler

et al., 2019) which allows imaging of mm wide slices. Such slices can be produced using hot-knife techniques (Hayworth et al., 2015), currently employed in preparation for FIB-SEM imaging. The versatility of synchrotron X-ray imaging then allows to rapidly acquire overview images followed by repeated targeted high-resolution image acquisition (Holler *et al.*, 2019). Alternatively or additionally, reconstruction algorithms taking multiple scattering events into account ("multi-slice ptychography", (Kahnt et al., 2021; Li and Maiden, 2018; Tsai et al., 2019)) are expected to improve data quality in particular for larger samples, reduce acquisition times(Jacobsen, 2018) and allow for extended geometries.

Currently, the speed of ptychographic tomography data collection is insufficient for connectome mapping studies; in our case a ~0.5×10^4 μm^3 tomogram volume was acquired in several hours. At this point, however, acquisition speed and volume are predominantly limited by coherent flux. As discussed previously (Holler *et al.*, 2017a), we expect significant improvements with the advent of fourth generation synchrotrons which will benefit from 1-2 orders of magnitude increased coherent X-ray flux (Yabashi and Tanaka, 2017). Furthermore, improvements in X-ray optics, such as replacing monochromators with multilayer mirrors (Bilderback et al., 1983) and Fresnel zone plates with Kirkpatrick-Baetz mirrors (Kirkpatrick and Baez, 1948; Morawe et al., 2015) or multilayer Laue lenses (Bajt et al., 2018; Li et al., 2023; Murray et al., 2019) can increase coherent flux by another 30-100 fold. Together with improved beam stability and improved detection systems that can maximally utilise increased flux, the upcoming innovations have the potential to improve overall acquisition speed by more than 4 orders of magnitude, putting non-destructive synaptic resolution imaging of cubic millimetre volumes well into the realm of standard beamtimes (Du *et al.*, 2021).

Here, we demonstrate that X-ray coherent imaging can densely resolve key connectomic features such as synapses in tissue. Future developments around staining, X-ray sources, computational reconstruction methods, and instrumentation will introduce this fundamentally non-destructive and highly reliable technique as a powerful contributor to the connectomics toolbox.

Figures and legends

Figure 1: X-ray ptychography of brain tissue

(a) Ptychography setup; top right: incoming coherent beam is focused by a lens to define the illumination onto the sample; center: cryogenic stage for scanning with 10 nm accuracy with a rotation stage; top left: SEM image of sample; bottom left: example diffraction pattern

(b) Single reconstructed phase projection.

(c) 3D rendering of a reconstructed 3D tomogram of olfactory bulb tissue

Figure 2: Dose-dependence of resolution for X-ray ptychography of brain tissue

(a1-a3) Example 2D slices for increasing radiation dose from conventional rigid tomography reconstruction

(b1-b3) Same reslices as in (a1-a3) with non-rigid tomographic reconstruction

(c-e) Fourier shell correlation (FSC) for the three radiation doses from (a,b). Solid line: rigid tomography reconstruction; dashed line: non-rigid tomographic reconstruction

(f) Resolution estimated by FSC in (c-e) as a function of dose. Solid and dashed lines indicate rigid and non-rigid tomographic reconstruction, respectively.

Figure 3: Subcellular features detectable with X-ray ptychography in different brain tissues

(a-d) Cutout views for X-ray ptychography tomographic reconstructions for different tissues (at radiation doses of 3.8×10^8 Gy, 3.8×10^8 Gy, 2.2×10^8 Gy, 1.9×10^8 Gy). Subcellular features including dendrites (green), nuclei (blue) and mitochondria (red) are resolved.

Figure 4: Quantitative evaluation of synapse detectability with correlative X-ray ptychography and FIB-SEM

(a) Schematic of workflow from PXCT to FIB-SEM

(b) Example PXCT image of a synapse in 3 orthogonal slices from the external plexiform layer of the OB. Note the prominent synapse in the center

(c) Same region from corresponding FIB-SEM image

(d) 5 dendrite branches traced in PXCT and FIB-SEM with synapses highlighted that were detected in both (orange squares, n=225) or in FIB-SEM only (gray squares, n=113)

(e) In an independent analysis, presence or absence of synapses was evaluated in n=240 randomly selected 1 μm^3 subvolumes in both FIB-SEM and PXCT volumes. The box plot indicates the average score given to the distinct ROIs, binned by their EM scores.

Figure 5: The tri-functional epoxy resin ("TF (tough) resin") for increased radiation resistance

(a) Chemical structure of the tri-functionalized TF (tough) resin (TF). TF consists of the tri-functional epoxy TGPAP and the amine curing agent DDM.

(b) Log-log plot of the increase in achieved resolution measured using Fourier Shell Correlation (FSC) as a function of the cumulative dose in two TR embedded pillars of 10 µm diameter. Arrow: Using non-rigid tomogram reconstruction, the final resolution at a dose of 2.5×10^9 Gy increased from 42.4 nm to 38.2 nm (red dot).

(c) The infiltration quality and the ultrastructural integrity for the TF embedded samples was assessed at high resolution using FIB-SEM after PXCT. The dark blue star indicates the location of the dark blue segmented neurite in (d). Left scale bar: 1 µm, right scale bar: 2 µm.

(d) Left: Side view of the pillar in (c) overlaid with some neurites that have been segmented using the PXCT data only. The dark blue neurite corresponds to the neurite labelled with a star in (c) and the light blue neurites correspond to some of its presynaptic partners. Right: Mitochondria and vesicle clusters segmented using the PXCT data only. Scale bar: 2 µm.

Supp Fig 2.1 - Radiation-induce deformation and non-rigid reconstructions

(a-b) Phase map of a single projection across the same sample position at the beginning (a) and at the end (b) of the tomogram. Note that the sample's width has increased during the tomogram acquisition, as illustrated below.

(c-d) Cross-section of the reconstructed tomogram using a rigid reconstruction algorithm. A region of interest is magnified in (d).

(e-f) Cross-section (e) and close-up view (f) of the same region as in (c-d), but reconstructed using a non-rigid algorithm. Finer details of biological features can be observed, in agreement with the improved FSC resolution.

Supp Fig 2.2 - Dose-dependent resolution measurements

(a1-a5) FRC obtained from 2D PXCT images obtained across different X-ray doses on multiple samples from three mouse brain tissue regions (EPL, RAD, CX).

(b) Resolution estimates for all scans in (a1-a5).

Supp Fig 2.3 - Radiation-induced mass loss

(a) Cross-section of two tomograms obtained from the same sample, reporting its ultrastructure after having been irradiated with an accumulated X-ray dose of 5×10^8 Gy and 13×10^8 Gy, respectively. Note the appearance of low electron density areas in the latter dataset (asterisks).

(b) Accumulated dose at which such mass loss damage was observed in the different samples embedded in Epon.

(c-d) Radiation-induced mass loss, measured in the central 2µm cross-section of each tomogram for all the tomogram history of the different samples. It is shown as absolute values (c) as well as relative to the first tomogram (d).

Supp Fig 4.1 - FIB-SEM investigation of ultrastructure

(a) 3D render of a sample imaged with both PXCT (blue) and FIB-SEM (gray). A 4x4 grid of column ROIs (green) was defined to annotate sample defects of two categories: curtains (blue) and bubbles (red).
(b) Distribution of the two artefact types inside and outside the PXCT-imaged region, suggesting X-ray irradiation as the cause for their appearance.
(c-d) Cross-section of the FIB-SEM dataset at two heights, showing bubble (c, asterisks) and curtain (d, arrowheads) artefacts.
(e-f) Close-up views of bubble (e) and curtain (f) artefacts.

Supp Fig 4.2 - Synapse detection in PXCT

(a) Cross-section of a sample imaged by both PXCT and FIB-SEM, showing the same plane viewed by either imaging modality.
(b) Spatial distribution of 250 non-overlapping regions of interest in the PXCT dataset's space coordinates, each region occupying 1 µm3 (blue) and 10 regions used for training (red).
(c) Synapse 'captcha' detection task: a human annotator is presented with each region of interest, displaying either the PXCT or FIB-SEM volume, and must annotate whether the region contains a synapse (score = 4) or it doesn't (score=1).
(d) All responses could be obtained from 3 human tracers across 240 regions of interest, and overall the scores distributed equally regardless of imaging modality.
(e-f) Confusion matrices of synapse detectability in PXCT using FIB-SEM as ground truth, showing all 4-categories (e) and pooling the results into 2 categories (f).

Supp Video 5.1 - Tomogram of TF embedded sample with resolution 38 nm

Supp Video 5.2 - 3D rendering of tomogram with segmented features

Materials & Methods

Animals: Animals used in this study were 8-13 week old wildtype mice of C57Bl/6 background of either sex. All animal protocols were approved by the Ethics Committee of the board of the Francis Crick Institute and the United Kingdom Home Office under the Animals (Scientific Procedures) Act 1986.

Tissue preparation

Tissue was prepared as described previously (Bosch *et al.*, 2022; Zhang *et al.*, 2022)

Dissection. Mice were sacrificed and 600 µm thick sections of brain areas of interest were sliced in ice-cold dissecting buffer (phosphate buffer 65 mM, 0.6 mM $CaCl_2$, 150 mM sucrose) with an osmolarity of 300 ± 10 mOsm/L using a LeicaVT1200S vibratome and immediately transferred to ice-cold fixative (either 1% glutaraldehyde or 1.25% glutaraldehyde and 2.5% paraformaldehyde in 150 mM sodium cacodylate buffer pH 7.40, 300 mOsm/L). Samples were left in the same fixative overnight, at 4 °C. The fixative was then washed with wash buffer (150 mM sodium cacodylate pH 7.40, 300 mOsm/L) three times for 10 min at 4 °C. Overall, samples were kept in an ice-cold, osmolarity- checked buffer.

Staining, dehydration and embedding. Slabs were stained with heavy metals using an established ROTO protocol (Pallotto *et al.*, 2015) using an automated tissue processor (Leica EMTP). Briefly, they were first stained with reduced osmium (2% OsO4, 3% potassium ferrocyanide, 2 mM CaCl2 in wash buffer) for 2 h at 20 °C, followed with 1% thiocarbohydrazide (aq) at 60 °C for 50 min, 2% osmium (aq) for 2 h at 20 °C, and 1% uranyl acetate (aq) overnight at 4 °C. On the next day, the samples were further stained with lead aspartate for 2 h at 60 °C. Samples were washed with double-distilled water six times for 10 min at 20 °C between each staining step, except warmer washes before and after TCH (50 °C) and before LA (60 °C).

Samples were then dehydrated with increasing ethanol solutions (75, 90, 2 × 100%), transferred to propylene oxide, and infiltrated with hard epon mixed with propylene oxide in increasing concentrations (25, 50, 75, 2 × 100%). Finally, samples were polymerised individually into plastic moulds for 72 h at 70 °C. While final chemical composition is difficult to estimate (Ströh et al., 2021), overall density of the polymerised resin was 1.24 ± 0.01 g/ml (n = 15 blocks of resin).

Sample verification: To verify staining and sample integrity, all samples were imaged with a Zeiss Versa 510 laboratory-based micro-CT (Bosch *et al.*, 2022).

Pillar preparation: Subsequently, a cylindrical sample was extracted from the embedded tissue using a 30keV Ga-beam of 13nA on a Zeiss NVision 40 Gallium FIB-SEM at PSI. The integrated micromanipulator was used to mount the sample on the holder (Holler et al., 2017b) for the PXCT measurement. The region of the sample was defined before preparation based on the microCT imaging results (Bosch *et al.*, 2022). Samples were polished and trimmed to expose the histological layers of interest using a diamond knife (trim 90, Diatome). The pillars were shaped and fine polished with a 30keV Ga-beam of 1.5nA. The TF pillars were first pre-milled with *Preppy* (Holler et al., 2020a). Fine polishing was performed with a Ga-FIB-SEM (TFS Helios 600 i, ScopeM) iteratively with currents decreasing from 65 nA to a final 2.5 nA (Fig 1a).

Tough resin protocol: After staining and dehydrating the samples as described above, the samples have been immersed in 2 x 100% acetonitrile (EMS-10020-450ML) for 30 min and 60 min, respectively. The tough resin (TF) consists of the tri-functional epoxy resin triglycidyl-p-aminophenol (TGPAP) and the hardener 4,4'-diaminodiphenylmethane (DDM) at weight ratio of DDM : TGPAP = 1:2. Because DDM does not mix well with TGPAP at room temperature and in order to facilitate the infiltration, DDM was first dissolved in acetonitrile heated to 70°C and subsequently, TGPAP was added. The samples were incubated in 1:3 TF : acetonitrile for 2 hrs at room temperature, 1:1 TF acetonitrile for 2-24 hrs at room temperature and subsequently the samples were placed in 1:1 TF : acetonitrile and cured for 12-72 hrs at 80°C. Because the boiling point of acetonitrile is at 82°C it is important to keep the sample container lid sufficiently open such that the acetonitrile can evaporate during the curing process.

Ptychography

Instrumentation: For all PXCT results shown here, we employed the OMNY instrument, depicted in Fig. 1 and described in full detail elsewhere (Holler, 2018 #1223}. The experiment was carried out at the cSAXS beamline of the Swiss Light Source (SLS) at the Paul Scherrer Institute, Villigen, Switzerland. Details of the components are as follows. Coherent X-rays enter the instrument and pass optical elements that in their combination form an X-ray lens used to generate a defined illumination onto the sample. These elements are a gold central stop, a Fresnel zone plate (FZP) and an order sorting aperture. The diffracted X-rays are measured by a 2D detector (Eiger 1.5M, (Dinapoli et al., 2011)). Accurate sample positioning is essential in X-ray ptychography and is achieved by horizontal and vertical interferometers that measure the relative position of the sample with respect to the beam-defining optics (Holler and Raabe, 2015). For this the sample is directly mounted on a reference mirror which is installed on a 3D piezo stage used for scanning the sample in the beam. A rotation stage allows recording projections at different orientations.

For the experimental description we distinguish between the different datasets analysed in this work. First, we have the samples embedded in Epon resin with a diameter of about 20 µm, shown in Figs. 2, 2.1, 2.2, 2.3, 3, 4, 4.1 and 4.2. Among these we call dataset 1 the one shown in Figs. 4 and 4.1, which was measured subsequently by FIBSEM and was used for the synapse identification. We then have the samples embedded in TF, which had a diameter of about 10 µm, used for the resolution plot in Fig. 5(b). One of these samples, imaged with a resolution of 38.2 nm, is shown in Fig. 5 and is referred to as dataset 2.

All measurements were performed at a photon energy of 6.2 keV corresponding to a wavelength of 2 Å selected using a fixed-exit double-crystal Si(111) monochromator. For the measurement of the Epon-resin samples, the FZP had a diameter of 220 µm and 60 nm outermost zone width, resulting in a focal distance of 66.0 mm, while for the TF samples we used a FZP with 250 µm diameter and 30 nm outermost zone width, which had a focal distance of 37.5 mm. Both FZPs featured locally displaced zones, designed to produce an optimal illumination for ptychography (Odstrcil et al., 2019c), and resulted in a beam flux of about 7×10^{8} photons/s. The undiffracted beam was blocked by the combination of a 40 µm diameter central stop and a 30 µm diameter order sorting aperture. The FZP was coherently illuminated by using an upstream slit of 20 µm horizontal width used as a secondary source. The detector was placed at about 7.2 m downstream of the sample.

Data acquisition: The samples were placed after the focal spot where the beam had a diameter of approximately 8 µm and 5 µm for the Epon- and TF-embedded samples,

respectively. In general, ptychographic scans were performed with a field of view that included the full sample size in the horizontal direction, while the scan points were positioned following a Fermat's spiral trajectory (Huang et al., 2014). The dose on each 2D ptychographic projection was adjusted by combining different acquisition settings, namely: (1) the average step size of the scan, ranging from 2.0 to 1.2 µm for the resin- or 1.4 to 0.5 µm for the TF-embedded samples, and (2) the exposure time at each scan point, ranging from 0.025 to 0.1 s. The settings for the most extensively analysed datasets were 1.2 and 0.5 µm step size for dataset 1 and 2, and 0.1 s exposure time. The vertical field of view of dataset 1 was 20 µm, while that for dataset 2 was 5 µm.

For the reconstruction of the Epon-embedded samples a detector area ranging from of 480 × 480 to 512 × 512 pixels was used, resulting in a reconstructed image pixel size of between 37.5 (which is the one for dataset 1) to 40.0 nm. For the TF samples we used 700 × 700 pixels on the detector, resulting in a reconstructed pixel size of 27.6 nm. Ptychographic reconstructions were performed with a few hundred iterations of the difference map (DM) algorithm followed by a few hundred iterations of a maximum likelihood (ML) refinement (Thibault and Guizar-Sicairos, 2012) in the case of the Epon-embedded samples. The reconstructions of the TF samples were performed with 2 probe modes using 600 iterations of ML.

For the tomography, several projections with equal angular spacing between sample rotations of 0° and 180° were recorded. The number of projections was varied between approximately 300 to 1200 as yet another parameter to adjust the the dose in PXCT datasets. The number of projections used for datasets 1 and 2 were 614 and 1190, respectively. For tomography, the phase of the reconstructed projections was used after post-processing alignment and removal of constant and linear phase components (Guizar-Sicairos et al., 2011; Odstrcil et al., 2019a). A modified filtered back projection was used after aligning the projections using a tomographic consistency approach (Guizar-Sicairos *et al.*, 2011). The tomograms were computed with a Hann or a RamLak filter for the Epon- and TF-embedded samples, respectively. For non-rigid reconstruction, we employed the algorithm described in (Odstrcil *et al.*, 2019b).

Dose estimation: We estimated the dose as the total energy absorbed by the sample divided by the total mass of the sample. For this the total number of photons absorbed were determined directly from the diffraction patterns, comparing with measurements where the beam is not going through the sample. For this measurement we relied on the linearity of the Eiger 1.5 M detector at maximum measured count rates of 10^5 photons/(s·pixel) and on its close to 100% efficiency at the used photon energy of 6.2 keV. The sample mass was estimated from the measured volume and the total number of electrons in the sample, which is measured directly by PXCT. For the conversion from the total number of electrons to total mass we made an estimation of the sample composition based on all the materials used for staining and on the composition of the EPON embedding resin, obtaining a molecular mass of about (1.9±0.1) g/mol, where the error stems from the uncertainty in the sample composition. The error in the determination of the absorbed dose is mostly given by this uncertainty.

FIB-SEM data acquisition

Focused ion beam scanning electron microscopy (FIB-SEM) was carried out using a Crossbeam 540 FIB-SEM with Atlas 5 for 3-dimensional tomography acquisition (Zeiss, Cambridge). The OMNY pin was coated with a 10 nm layer of platinum, mounted

horizontally on a standard 12.7 mm SEM stub using carbon cement (LeitC), and coated with a further 10 nm layer of platinum. This method of mounting the pin ensured the cylinder of tissue was positioned in free space and could be reoriented appropriately within the SEM for ion beam milling with consideration to the X-ray dataset. As the sample was cylindrical and tracking marks therefore could not be applied, direct tracking of slice thickness was not possible. Autofocus and autostigmation functions were carried out on an area close to the outer edge of the sample. Electron micrographs were acquired at either 8 nm or 4 nm isotropic resolution, using a 12 µs or 9 µs dwell time, respectively. During acquisition, the SEM was operated at an accelerating voltage of 1.5 kV with 1 nA current. The EsB detector was used with a grid voltage of 1,200 V. Ion beam milling was performed at an accelerating voltage of 30 kV and current of 700 pA. Approximate data acquisition times were at 8 nm voxel size – 3 days 7 hours, 3260 slices and at 4 nm – 1 day 14 hours, 1360 slices.
The FIB-SEM dataset was later warped to the ptychography space using Bigwarp (Bogovic et al., 2016). The warped data of the volume also imaged with ptychography was then exported to the ptychography dataset's space with a voxel size of 9.4 nm in x,y,z (which is 1/4 of the voxel size of the native ptychography dataset, 37.6 nm). In this way, both datasets could be stored as different layers of a common dataset in webknossos (Boergens et al., 2017). This setup enabled quick toggling between imaging modalities at any particular location, and simplified the configuration of the synapse detection tasks.

Data analysis

FSC analysis:

To measure resolution, a custom implementation of Fourier ring or shell correlation analysis was used. For the estimation of the 2D resolution of a projection image, we perform the 2D Fourier ring correlation (FRC) between that image and a second image acquired with identical experimental parameters. We then compare the FRC with a threshold using the 1-bit criterion, which is equivalent to a signal to noise ratio of 0.5 for each of the compared images(van Heel and Schatz, 2005). This procedure provides an estimation of the half-pitch resolution for each of the individual images. For the estimation of the 3D resolution of a tomographic dataset, we compute the 3D Fourier shell correlation (FSC) of two subtomograms, each computed using half of the tomographic projections. In this way, we obtain two datasets acquired independently, albeit each with double angular sampling. We then compare the FSC with a threshold according to the ½-bit criterion, which corresponds to a signal to noise ratio of 0.4 for the full tomographic dataset.

Synapse identification:

The synapse identification tasks were performed on the sample for which both FIB-SEM as well as Ptychography data was available.
Two synapse identification approaches are presented: a dendrite-centric one and a randomised "captcha"-like detection.
For the dendrite-centric synapse identification task, five dendrites evolving in straight trajectories in distinct directions were chosen and traced (in a skeleton format) from the ground truth FIB-SEM dataset. The dendrites chosen all presented a pale cytoplasm, straight trajectory, no branches and consistent thickness of around 2 µm, to ensure they could be followed in the datasets of both imaging modalities. Since the sample this dataset belongs to was extracted from the external plexiform layer of the olfactory bulb, these dendrites are likely to be lateral (and possibly apical) dendrites of projection neurons (mitral or tufted

cells). Each dendrite skeleton was followed three times independently looking at one orthogonal plane only, and every time all features resembling synapses were annotated by seeding single nodes. This operation was performed for both the FIB-SEM as well as the ptychography dataset (n = 725 initial nodes in FIB-SEM, 576 initial nodes in PXCT). All nodes seeded in the FIB-SEM dataset were assumed to be pointing to true synapses. Based on previous studies, synapse density was estimated to be of 1-2 synapse / μm^3 (Santuy et al., 2020). First, we obtained a census of synapses by looking at the FIB-SEM data alone: nodes seeded ≤ 300 nm away from each other were assumed to be pointing to the same synapse, which lead to a total census of 338 synapses in all 5 dendrites. Most synapses (273/338, 81%) were detected on the first pass in the FIB-SEM dataset, and only a small fraction of the final census was only found at the 3rd and last pass (65/338, 19%), consistent with the assumption that synapses are well resolved in the FIB-SEM data. Next, the nodes seeded in the ptychography dataset were matched with the previously defined census of synapses through a similar process: FIB-SEM-validated synapse locations receiving a tag from the ptychography dataset within a 300 nm euclidean distance were marked as 'detected'. Most detected synapses in X-rays (148/225, 66%) were already detected on the first pass in the ptychography dataset, and only a small fraction were only detected at the 2nd and last passes (77/225, 34%). A number of annotations of putative synapses in the ptychography datasets were not matched to any synapse. These annotations were further used to detect robust confounding factors when annotating synapses. Locations in the dataset receiving ≥ 2 tags within a ≤ 300 nm distance were defined as 'hot spots' for confusion. A total of 36 hotspots were detected, and their ultrastructure was revisited in the FIB-SEM dataset. Features providing the confusion were then identified by toggling the view of the ptychography and FIB-SEM dataset in the browser, and ultimately the nature of the feature leading to false positive detection in the ptychography dataset was annotated categorically. After revisiting the ultrastructure of all 36 false positive hotspots, we quantified the prevalence of the different feature categories.

For the "captcha"-like synapse detection task, we generated 250 non-overlapping and randomly located 1*1*1 μm^3 regions of interest (Supp Fig 4.2). These regions could be displayed as cubes with 3 red faces and 3 green faces in the webknossos environment. The task consisted in determining whether a given region contained a synapse or not, by assigning a confidence score of [1 = clearly not containing a synapse, 2, 3, 4 = clearly containing a synapse]. If the synapse was only partly contained inside the region, it would only be taken into account if it exits the region through a green boundary. Additionally, ten locations known to contain a synapse (extracted from the previous dendrite-centric analysis) were chosen as training data. Finally, the task was encoded within the webknossos ecosystem such as one would be navigated from region to region after each answer was being recorded, and only one dataset (the one being tested each time) would be presented (Supp Fig 4.2). The task, overall, consisted on exploring the X-ray and FIB-SEM appearance of 10 training synapses, then assess the presence of synapses in the 250 regions in the ptychography dataset, and then assess the presence of synapses in the 250 regions in the FIB-SEM dataset. Three independent annotators, all experts in the appearance of synapses when their fine ultrastructure is resolved (e.g. by FIB-SEM) ran the task. The analyses returned therefore a 250 regions x 3 annotators x 2 imaging modalities array of responses, each with a value of either [1, 2, 3, 4]. In some cases, some annotators did not log a response before switching to the next task, which provided a value of 0. Only regions with

correct assessments from all 3 annotators were kept, providing a cleaned up array of 240x3x2 responses. By matching region IDs, this array was represented in a 240x6 table and complemented with other regional metadata in additional columns. For every region, the average score from each imaging modality was calculated from all scores given by the three annotators. All 4 possible values were well represented in both imaging modalities (Supp Fig 4.3). At this point, table rows were split into 4 groups according to the average FIB-SEM scores of each region (rounded to the closest integer). This allowed plotting the scores assigned in the ptychography data depending on the score given in the FIB-SEM data at the same region (Fig 4(e)). The average responses of all regions in both modalities were later binned into two categories (average score ≤2 categorised as 'no synapse'; average score > 2 categorised as 'synapse'). This allowed extracting a confusion matrix on the detectability of synapses (Supp Fig 4.2).
The segmentation and renderings shown in Fig 1c, Fig 5d and Supp Video 5.2 have been generated using the image analysis services of https://ariadne.ai.

Acknowledgements
The authors are grateful to the biological research and scientific computing science technology platforms of the Francis Crick Institute and thank Ruairi Roberts for expert annotation of synapses. This research was funded in whole, or in part, by the Wellcome Trust (FC001153 and 110174/Z/15/Z to A.T.S.; FC001999 to L.M.C.). For the purpose of Open Access, the author has applied a CC BY public copyright licence to any Author Accepted Manuscript version arising from this submission. We acknowledge the Paul Scherrer Institut, Villigen, Switzerland, for provision of synchrotron radiation beamtime at the cSAXS beamline of the Swiss Light Source (proposals 20190654, , 20200783 and 20211852). The authors gratefully acknowledge ScopeM at ETHZ and in particular Joakim Reuteler for their support & assistance in this work. This work was supported by the Francis Crick Institute, which receives its core funding from Cancer Research UK (FC001153 to A.T.S.; FC001999 to L.C.), the UK Medical Research Council (FC001153 to A.T.S., FC001999 to L.C.), and the Wellcome Trust (FC001153 to A.T.S., FC001999 to L.C.). It was also supported by a Physics of Life grant (EP/W024292/1) to A.T.S. and A.P. funded by EPSRC and Wellcome. A.P. acknowledges funding from the European Research Council under the European Union's Horizon 2020 Research and Innovation Programme (852455). A.A.W. acknowledges funding from the SERI-funded ERCStG *XrayConnectomics*.

References

Abbott, L.F., Bock, D.D., Callaway, E.M., Denk, W., Dulac, C., Fairhall, A.L., Fiete, I., Harris, K.M., Helmstaedter, M., Jain, V., et al. (2020). The Mind of a Mouse. Cell *182*, 1372-1376. 10.1016/j.cell.2020.08.010.

Bajt, S., Prasciolu, M., Fleckenstein, H., Domaracky, M., Chapman, H.N., Morgan, A.J., Yefanov, O., Messerschmidt, M., Du, Y., Murray, K.T., et al. (2018). X-ray focusing with efficient high-NA multilayer Laue lenses. Light Sci Appl *7*, 17162. 10.1038/lsa.2017.162.

Beetz, T., and Jacobsen, C. (2003). Soft X-ray radiation-damage studies in PMMA using a cryo-STXM. Journal of Synchrotron Radiation *10*, 280-283. 10.1107/s0909049503003261.

Bilderback, D.H., Lairson, B.M., Barbee, T.W., Ice, G.E., and Sparks, C.J. (1983). Design of doubly focusing, tunable (5–30 keV), wide bandpass optics made from layered synthetic microstructures. Nuclear Instruments and Methods in Physics Research *208*, 251-261. 10.1016/0167-5087(83)91132-8.

Bock, D.D., Lee, W.C., Kerlin, A.M., Andermann, M.L., Hood, G., Wetzel, A.W., Yurgenson, S., Soucy, E.R., Kim, H.S., and Reid, R.C. (2011). Network anatomy and in vivo physiology of visual cortical neurons. Nature *471*, 177-182. 10.1038/nature09802.

Boergens, K.M., Berning, M., Bocklisch, T., Braunlein, D., Drawitsch, F., Frohnhofen, J., Herold, T., Otto, P., Rzepka, N., Werkmeister, T., et al. (2017). webKnossos: efficient online 3D data annotation for connectomics. Nature methods *14*, 691-694. 10.1038/nmeth.4331.

Bogovic, J.A., Hanslovsky, P., Wong, A., and Saalfeld, S. (2016). Robust registration of calcium images by learned contrast synthesis. 2016-04-01. (IEEE).

Bosch, C., Ackels, T., Pacureanu, A., Zhang, Y., Peddie, C.J., Berning, M., Rzepka, N., Zdora, M.C., Whiteley, I., Storm, M., et al. (2022). Functional and multiscale 3D structural investigation of brain tissue through correlative in vivo physiology, synchrotron microtomography and volume electron microscopy. Nature Communications *13*, 2923. 10.1038/s41467-022-30199-6.

Briggman, K.L., and Bock, D.D. (2012). Volume electron microscopy for neuronal circuit reconstruction. Current opinion in neurobiology *22*, 154-161. 10.1016/j.conb.2011.10.022.

Busse, M., Marciniszyn, J.P., Ferstl, S., Kimm, M.A., Pfeiffer, F., and Gulder, T. (2021). 3D-Non-destructive Imaging through Heavy-Metal Eosin Salt Contrast Agents. Chemistry – A European Journal *27*, 4561-4566. 10.1002/chem.202005203.

Cedola, A., Bravin, A., Bukreeva, I., Fratini, M., Pacureanu, A., Mittone, A., Massimi, L., Cloetens, P., Coan, P., Campi, G., et al. (2017). X-Ray Phase Contrast Tomography Reveals Early Vascular Alterations and Neuronal Loss in a Multiple Sclerosis Model. Sci Rep *7*. 10.1038/s41598-017-06251-7.

Cloetens, P., Ludwig, W., Baruchel, J., Van Dyck, D., Van Landuyt, J., Guigay, J.P., and Schlenker, M. (1999). Holotomography: Quantitative phase tomography with micrometer resolution using hard synchrotron radiation x rays. Appl Phys Lett *75*, 2912-2914. 10.1063/1.125225.

Denk, W., and Horstmann, H. (2004). Serial block-face scanning electron microscopy to reconstruct three-dimensional tissue nanostructure. PLoS biology *2*, e329. 10.1371/journal.pbio.0020329.

Dinapoli, R., Bergamaschi, A., Henrich, B., Horisberger, R., Johnson, I., Mozzanica, A., Schmid, E., Schmitt, B., Schreiber, A., Shi, X., and Theidel, G. (2011). EIGER: Next generation single photon counting detector for X-ray applications. Nuclear Instruments and Methods in

Physics Research Section A: Accelerators, Spectrometers, Detectors and Associated Equipment *650*, 79-83. 10.1016/j.nima.2010.12.005.
Du, M., Di, Z., Gürsoy, D., Xian, R.P., Kozorovitskiy, Y., and Jacobsen, C. (2021). Upscaling X-ray nanoimaging to macroscopic specimens. J Appl Crystal *54*, 386-401. 10.1107/s1600576721000194.
Du, M., and Jacobsen, C. (2018). Relative merits and limiting factors for x-ray and electron microscopy of thick, hydrated organic materials. Ultramicroscopy *184*, 293-309. 10.1016/j.ultramic.2017.10.003.
Dyer, E.L., Gray Roncal, W., Prasad, J.A., Fernandes, H.L., Gursoy, D., De Andrade, V., Fezzaa, K., Xiao, X., Vogelstein, J.T., Jacobsen, C., et al. (2017). Quantifying Mesoscale Neuroanatomy Using X-Ray Microtomography. eNeuro *4*. 10.1523/ENEURO.0195-17.2017.
Fonseca, M.C., Araujo, B.H.S., Dias, C.S.B., Archilha, N.L., Neto, D.P.A., Cavalheiro, E., Westfahl, H., Jr., da Silva, A.J.R., and Franchini, K.G. (2018). High-resolution synchrotron-based X-ray microtomography as a tool to unveil the three-dimensional neuronal architecture of the brain. Sci Rep *8*, 12074. 10.1038/s41598-018-30501-x.
Gao, R., Asano, S.M., Upadhyayula, S., Pisarev, I., Milkie, D.E., Liu, T.L., Singh, V., Graves, A., Huynh, G.H., Zhao, Y., et al. (2019). Cortical column and whole-brain imaging with molecular contrast and nanoscale resolution. Science *363*. 10.1126/science.aau8302.
Grishina, D.A., Harteveld, C.A.M., Pacureanu, A., Devashish, D., Lagendijk, A., Cloetens, P., and Vos, W.L. (2019). X-ray Imaging of Functional Three-Dimensional Nanostructures on Massive Substrates. ACS Nano *13*, 13932-13939. 10.1021/acsnano.9b05519.
Guizar-Sicairos, M., Diaz, A., Holler, M., Lucas, M.S., Menzel, A., Wepf, R.A., and Bunk, O. (2011). Phase tomography from x-ray coherent diffractive imaging projections. Opt Express *19*, 21345-21357. 10.1364/OE.19.021345.
Guizar-Sicairos, M., Johnson, I., Diaz, A., Holler, M., Karvinen, P., Stadler, H.C., Dinapoli, R., Bunk, O., and Menzel, A. (2014). High-throughput ptychography using Eiger: scanning X-ray nano-imaging of extended regions. Opt Express *22*, 14859-14870. 10.1364/OE.22.014859.
Harauz, G., and van Heel, M. (1986). Exact filters for general geometry three dimensional reconstruction. Optik *73*, 146-156.
Hayworth, K.J., Morgan, J.L., Schalek, R., Berger, D.R., Hildebrand, D.G., and Lichtman, J.W. (2014). Imaging ATUM ultrathin section libraries with WaferMapper: a multi-scale approach to EM reconstruction of neural circuits. Front Neural Circuits *8*, 68. 10.3389/fncir.2014.00068.
Hayworth, K.J., Peale, D., Januszewski, M., Knott, G.W., Lu, Z., Xu, C.S., and Hess, H.F. (2020). Gas cluster ion beam SEM for imaging of large tissue samples with 10 nm isotropic resolution. Nature methods *17*, 68-71. 10.1038/s41592-019-0641-2.
Hayworth, K.J., Xu, C.S., Lu, Z., Knott, G.W., Fetter, R.D., Tapia, J.C., Lichtman, J.W., and Hess, H.F. (2015). Ultrastructurally smooth thick partitioning and volume stitching for large-scale connectomics. Nat Meth *12*, 319-322. 10.1038/nmeth.3292.
Helfen, L., Baumbach, T., Mikulík, P., Kiel, D., Pernot, P., Cloetens, P., and Baruchel, J. (2005). High-resolution three-dimensional imaging of flat objects by synchrotron-radiation computed laminography. Appl Phys Lett *86*. 10.1063/1.1854735.
Helfen, L., Xu, F., Suhonen, H., Urbanelli, L., Cloetens, P., and Baumbach, T. (2013). Nano-laminography for three-dimensional high-resolution imaging of flat specimens. Journal of Instrumentation *8*, C05006-C05006. 10.1088/1748-0221/8/05/c05006.
Helmstaedter, M. (2013). Cellular-resolution connectomics: challenges of dense neural circuit reconstruction. Nature methods *10*, 501-507. 10.1038/nmeth.2476.

Henderson, R. (1995). The potential and limitations of neutrons, electrons and X-rays for atomic resolution microscopy of unstained biological molecules. Quarterly Reviews of Biophysics *28*, 171-193. 10.1017/s003358350000305x.
Heymann, J.A., Hayles, M., Gestmann, I., Giannuzzi, L.A., Lich, B., and Subramaniam, S. (2006). Site-specific 3D imaging of cells and tissues with a dual beam microscope. J Struct Biol *155*, 63-73. 10.1016/j.jsb.2006.03.006.
Holler, M., Guizar-Sicairos, M., Tsai, E.H., Dinapoli, R., Muller, E., Bunk, O., Raabe, J., and Aeppli, G. (2017a). High-resolution non-destructive three-dimensional imaging of integrated circuits. Nature *543*, 402-406. 10.1038/nature21698.
Holler, M., Ihli, J., Tsai, E.H.R., Nudelman, F., Verezhak, M., van de Berg, W.D.J., and Shahmoradian, S.H. (2020a). A lathe system for micrometre-sized cylindrical sample preparation at room and cryogenic temperatures. J Synchrotron Radiat *27*, 472-476. 10.1107/S1600577519017028.
Holler, M., Odstrcil, M., Guizar-Sicairos, M., Lebugle, M., Frommherz, U., Lachat, T., Bunk, O., Raabe, J., and Aeppli, G. (2020b). LamNI - an instrument for X-ray scanning microscopy in laminography geometry. J Synchrotron Radiat *27*, 730-736. 10.1107/S1600577520003586.
Holler, M., Odstrcil, M., Guizar-Sicairos, M., Lebugle, M., Müller, E., Finizio, S., Tinti, G., David, C., Zusman, J., Unglaub, W., et al. (2019). Three-dimensional imaging of integrated circuits with macro- to nanoscale zoom. Nature Electronics *2*, 464-470. 10.1038/s41928-019-0309-z.
Holler, M., and Raabe, J. (2015). Error motion compensating tracking interferometer for the position measurement of objects with rotational degree of freedom. Optical Engineering *54*. 10.1117/1.Oe.54.5.054101.
Holler, M., Raabe, J., Diaz, A., Guizar-Sicairos, M., Quitmann, C., Menzel, A., and Bunk, O. (2012). An instrument for 3D x-ray nano-imaging. Review of Scientific Instruments *83*. 10.1063/1.4737624.
Holler, M., Raabe, J., Diaz, A., Guizar-Sicairos, M., Wepf, R., Odstrcil, M., Shaik, F.R., Panneels, V., Menzel, A., Sarafimov, B., et al. (2018). OMNY-A tOMography Nano crYo stage. Rev Sci Instrum *89*, 043706. 10.1063/1.5020247.
Holler, M., Raabe, J., Wepf, R., Shahmoradian, S.H., Diaz, A., Sarafimov, B., Lachat, T., Walther, H., and Vitins, M. (2017b). OMNY PIN-A versatile sample holder for tomographic measurements at room and cryogenic temperatures. Rev Sci Instrum *88*, 113701. 10.1063/1.4996092.
Horstmann, H., Korber, C., Satzler, K., Aydin, D., and Kuner, T. (2012). Serial section scanning electron microscopy (S3EM) on silicon wafers for ultra-structural volume imaging of cells and tissues. PloS one *7*, e35172. 10.1371/journal.pone.0035172.
Howells, M.R., Beetz, T., Chapman, H.N., Cui, C., Holton, J.M., Jacobsen, C.J., Kirz, J., Lima, E., Marchesini, S., Miao, H., et al. (2009). An assessment of the resolution limitation due to radiation-damage in x-ray diffraction microscopy. J Electron Spectros Relat Phenomena *170*, 4-12. 10.1016/j.elspec.2008.10.008.
Hua, Y., Laserstein, P., and Helmstaedter, M. (2015). Large-volume en-bloc staining for electron microscopy-based connectomics. Nature communications *6*, 7923. 10.1038/ncomms8923.
Huang, B., Bates, M., and Zhuang, X. (2009). Super-resolution fluorescence microscopy. Annu Rev Biochem *78*, 993-1016. 10.1146/annurev.biochem.77.061906.092014.

Huang, X., Yan, H., Harder, R., Hwu, Y., Robinson, I.K., and Chu, Y.S. (2014). Optimization of overlap uniformness for ptychography. Opt Express *22*, 12634-12644. 10.1364/OE.22.012634.
Igarashi, M., Nozumi, M., Wu, L.G., Cella Zanacchi, F., Katona, I., Barna, L., Xu, P., Zhang, M., Xue, F., and Boyden, E. (2018). New observations in neuroscience using superresolution microscopy. The Journal of neuroscience : the official journal of the Society for Neuroscience *38*, 9459-9467. 10.1523/JNEUROSCI.1678-18.2018.
Jacobsen, C. (2018). Relaxation of the Crowther criterion in multislice tomography. Optics Letters *43*, 4811. 10.1364/ol.43.004811.
Januszewski, M., Kornfeld, J., Li, P.H., Pope, A., Blakely, T., Lindsey, L., Maitin-Shepard, J., Tyka, M., Denk, W., and Jain, V. (2018). High-precision automated reconstruction of neurons with flood-filling networks. Nat Meth *15*, 605-610. 10.1038/s41592-018-0049-4.
Kahnt, M., Grote, L., Brückner, D., Seyrich, M., Wittwer, F., Koziej, D., and Schroer, C.G. (2021). Multi-slice ptychography enables high-resolution measurements in extended chemical reactors. Sci Rep *11*. 10.1038/s41598-020-80926-6.
Karlupia, N., Schalek, R.L., Wu, Y., Meirovitch, Y., Wei, D., Charney, A.W., Kopell, B.H., and Lichtman, J.W. (2023). Immersion fixation and staining of multi-cubic millimeter volumes for electron microscopy-based connectomics of human brain biopsies. Biol Psychiatry. 10.1016/j.biopsych.2023.01.025.
Kasthuri, N., Hayworth, K.J., Berger, D.R., Schalek, R.L., Conchello, J.A., Knowles-Barley, S., Lee, D., Vazquez-Reina, A., Kaynig, V., Jones, T.R., et al. (2015). Saturated Reconstruction of a Volume of Neocortex. Cell *162*, 648-661. 10.1016/j.cell.2015.06.054.
Khimchenko, A., Pacureanu, A., Bikis, C., Hieber, S.E., Thalmann, P., Deyhle, H., Schweighauser, G., Hench, J., Frank, S., Müller-Gerbl, M., et al. (2018). Hard X-ray Nano-Holotomography of Formalin-Fixated and Paraffin-Embedded Human Brain Tissue. Microscopy and Microanalysis *24*, 354-355. 10.1017/s143192761801406x.
Kirkpatrick, P., and Baez, A.V. (1948). Formation of optical images by X-rays. J Opt Soc Am *38*, 766-774. 10.1364/josa.38.000766.
Klinger, E., Motta, A., Marr, C., Theis, F.J., and Helmstaedter, M. (2021). Cellular connectomes as arbiters of local circuit models in the cerebral cortex. Nature Communications *12*. 10.1038/s41467-021-22856-z.
Knott, G., Marchman, H., Wall, D., and Lich, B. (2008). Serial Section Scanning Electron Microscopy of Adult Brain Tissue Using Focused Ion Beam Milling. J Neurosci *28*, 2959-2964. 10.1523/jneurosci.3189-07.2008.
Kornfeld, J., and Denk, W. (2018). Progress and remaining challenges in high-throughput volume electron microscopy. Curr Opin Neurobiol *50*, 261-267. 10.1016/j.conb.2018.04.030.
Kuan, A.T., Phelps, J.S., Thomas, L.A., Nguyen, T.M., Han, J., Chen, C.L., Azevedo, A.W., Tuthill, J.C., Funke, J., Cloetens, P., et al. (2020). Dense neuronal reconstruction through X-ray holographic nano-tomography. Nat Neurosci *23*, 1637. 10.1038/s41593-020-0704-9.
Li, P., and Maiden, A. (2018). Multi-slice ptychographic tomography. Sci Rep *8*. 10.1038/s41598-018-20530-x.
Li, T., Dresselhaus, J.L., Ivanov, N., Prasciolu, M., Fleckenstein, H., Yefanov, O., Zhang, W., Pennicard, D., Dippel, A.-C., Gutowski, O., et al. (2023). Dose-efficient scanning Compton X-ray microscopy. Light: Science & Applications *12*. 10.1038/s41377-023-01176-5.
Lichtman, J.W., and Sanes, J.R. (2008). Ome sweet ome: what can the genome tell us about the connectome? Current opinion in neurobiology *18*, 346-353. 10.1016/j.conb.2008.08.010.

Litwin-Kumar, A., and Turaga, S.C. (2019). Constraining computational models using electron microscopy wiring diagrams. Current opinion in neurobiology *58*, 94-100. 10.1016/j.conb.2019.07.007.
Lu, X., Wu, Y., Schalek, R.L., Meirovitch, Y., Berger, D.R., and Lichtman, J.W. (2023). A Scalable Staining Strategy for Whole-Brain Connectomics. bioRxiv. 10.1101/2023.09.26.558265.
Michelson, A., Minevich, B., Emamy, H., Huang, X., Chu, Y.S., Yan, H., and Gang, O. (2022). Three-dimensional visualization of nanoparticle lattices and multimaterial frameworks. Science *376*, 203-207. 10.1126/science.abk0463.
Mikula, S., and Denk, W. (2015). High-resolution whole-brain staining for electron microscopic circuit reconstruction. Nature methods *12*, 541-546. 10.1038/nmeth.3361.
Mizutani, R., Saiga, R., Takeuchi, A., Uesugi, K., and Suzuki, Y. (2013). Three-dimensional network of Drosophila brain hemisphere. Journal of Structural Biology *184*, 271-279. 10.1016/j.jsb.2013.08.012.
Momose, A., Takeda, T., Itai, Y., and Hirano, K. (1996). Phase–contrast X–ray computed tomography for observing biological soft tissues. Nature Medicine *2*, 473-475. 10.1038/nm0496-473.
Morawe, C., Barrett, R., Cloetens, P., Lantelme, Peffen, and Vivo (2015). Graded multilayers for figured Kirkpatrick-Baez mirrors on the new ESRF end station ID16A. SPIE Optical Engineering+Applications. 10.1117/12.2189279.
Murray, K.T., Pedersen, A.F., Mohacsi, I., Detlefs, C., Morgan, A.J., Prasciolu, M., Yildirim, C., Simons, H., Jakobsen, A.C., Chapman, H.N., et al. (2019). Multilayer Laue lenses at high X-ray energies: performance and applications. Optics Express *27*, 7120. 10.1364/oe.27.007120.
Odstrcil, M., Holler, M., Raabe, J., and Guizar-Sicairos, M. (2019a). Alignment methods for nanotomography with deep subpixel accuracy. Opt Express *27*, 36637-36652. 10.1364/OE.27.036637.
Odstrcil, M., Holler, M., Raabe, J., Sepe, A., Sheng, X., Vignolini, S., Schroer, C.G., and Guizar-Sicairos, M. (2019b). Ab initio nonrigid X-ray nanotomography. Nature Communications *10*. 10.1038/s41467-019-10670-7.
Odstrcil, M., Lebugle, M., Guizar-Sicairos, M., David, C., and Holler, M. (2019c). Towards optimized illumination for high-resolution ptychography. Opt Express *27*, 14981-14997. 10.1364/OE.27.014981.
Pallotto, M., Watkins, P.V., Fubara, B., Singer, J.H., and Briggman, K.L. (2015). Extracellular space preservation aids the connectomic analysis of neural circuits. Elife *4*, e08206. 10.7554/eLife.08206.
Panneels, V., Diaz, A., Imsand, C., Guizar-Sicairos, M., Müller, E., Bittermann, A.G., Ishikawa, T., Menzel, A., Kaech, A., Holler, M., et al. (2021). Imaging of retina cellular and subcellular structures using ptychographic hard X-ray tomography. Journal of Cell Science *134*. 10.1242/jcs.258561.
Pfeiffer, F. (2018). X-ray ptychography. Nature Photonics *12*, 9-17. 10.1038/s41566-017-0072-5.
Phelps, J.S., Hildebrand, D.G.C., Graham, B.J., Kuan, A.T., Thomas, L.A., Nguyen, T.M., Buhmann, J., Azevedo, A.W., Sustar, A., Agrawal, S., et al. (2021). Reconstruction of motor control circuits in adult Drosophila using automated transmission electron microscopy. Cell *184*, 759-774.e718. 10.1016/j.cell.2020.12.013.
Reichardt, M., Moller Jensen, P., Andersen Dahl, V., Bjorholm Dahl, A., Ackermann, M., Shah, H., Länger, F., Werlein, C., Kuehnel, M.P., Jonigk, D., and Salditt, T. (2021). 3D virtual

histopathology of cardiac tissue from Covid-19 patients based on phase-contrast X-ray tomography. eLife *10*. 10.7554/elife.71359.
Reichmann, J., Ruhwedel, T., Mobius, W., and Salditt, T. (2023). Neodymium acetate as a contrast agent for X-ray phase-contrast tomography. J Med Imaging (Bellingham) *10*, 056001. 10.1117/1.JMI.10.5.056001.
Rodenburg, J., and Maiden, A. (2019). Ptychography. In Springer Handbook of Microscopy, pp. 2-2. 10.1007/978-3-030-00069-1_17.
Santuy, A., Tomás-Roca, L., Rodríguez, J.-R., González-Soriano, J., Zhu, F., Qiu, Z., Grant, S.G.N., Defelipe, J., and Merchan-Perez, A. (2020). Estimation of the number of synapses in the hippocampus and brain-wide by volume electron microscopy and genetic labeling. Sci Rep *10*. 10.1038/s41598-020-70859-5.
Schmidt, M., Motta, A., Sievers, M., and Helmstaedter, M. (2022). RoboEM: automated 3D flight tracing for synaptic-resolution connectomics. Cold Spring Harbor Laboratory.
Schulz, G., Weitkamp, T., Zanette, I., Pfeiffer, F., Beckmann, F., David, C., Rutishauser, S., Reznikova, E., and Müller, B. (2010). High-resolution tomographic imaging of a human cerebellum: comparison of absorption and grating-based phase contrast. Journal of The Royal Society Interface *7*, 1665-1676. 10.1098/rsif.2010.0281.
Shahmoradian, S.H., Tsai, E.H.R., Diaz, A., Guizar-Sicairos, M., Raabe, J., Spycher, L., Britschgi, M., Ruf, A., Stahlberg, H., and Holler, M. (2017). Three-Dimensional Imaging of Biological Tissue by Cryo X-Ray Ptychography. Scientific reports *7*, 6291. 10.1038/s41598-017-05587-4.
Song, K., Feng, Z., and Helmstaedter, M. (2022). High-contrast en-bloc staining of mouse whole-brain samples for EM-based connectomics. Cold Spring Harbor Laboratory.
Ströh, S., Hammerschmith, E.W., Tank, D.W., Seung, H.S., and Wanner, A.A. (2021). In situ X-ray assisted electron microscopy staining for large biological samples. bioRxiv, 2021.2006.2019.448808. 10.1101/2021.06.19.448808.
Thibault, P., and Guizar-Sicairos, M. (2012). Maximum-likelihood refinement for coherent diffractive imaging. New Journal of Physics *14*. 10.1088/1367-2630/14/6/063004.
Tonnesen, J., Inavalli, V., and Nagerl, U.V. (2018). Super-Resolution Imaging of the Extracellular Space in Living Brain Tissue. Cell *172*, 1108-1121 e1115. 10.1016/j.cell.2018.02.007.
Topperwien, M., van der Meer, F., Stadelmann, C., and Salditt, T. (2018). Three-dimensional virtual histology of human cerebellum by X-ray phase-contrast tomography. Proc Natl Acad Sci U S A *115*, 6940-6945. 10.1073/pnas.1801678115.
Tsai, E.H.R., Marone, F., and Guizar-Sicairos, M. (2019). Gridrec-MS: an algorithm for multi-slice tomography. Opt Lett *44*, 2181-2184. 10.1364/OL.44.002181.
Van De Voorde, M.E. (1970). Action of ionizing radiation on epoxy resins. Office of Scientific and Technical Information (OSTI). 1970-12-01.
van Heel, M., and Schatz, M. (2005). Fourier shell correlation threshold criteria. Journal of Structural Biology *151*, 250-262. 10.1016/j.jsb.2005.05.009.
Walsh, C.L., Tafforeau, P., Wagner, W.L., Jafree, D.J., Bellier, A., Werlein, C., Kühnel, M.P., Boller, E., Walker-Samuel, S., Robertus, J.L., et al. (2021). Imaging intact human organs with local resolution of cellular structures using hierarchical phase-contrast tomography. Nat Meth *18*, 1532-1541. 10.1038/s41592-021-01317-x.
Wu, Z., Zhang, H., Yang, H., Chu, X., Song, Y., Wu, W., Liu, H., and Li, L. (2011). Properties of radiation stable, low viscosity impregnating resin for cryogenic insulation system. Cryogenics *51*, 229-233. 10.1016/j.cryogenics.2010.06.007.

Xu, C.S., Hayworth, K.J., Lu, Z., Grob, P., Hassan, A.M., Garcia-Cerdan, J.G., Niyogi, K.K., Nogales, E., Weinberg, R.J., and Hess, H.F. (2017). Enhanced FIB-SEM systems for large-volume 3D imaging. Elife *6*. 10.7554/eLife.25916.
Yabashi, M., and Tanaka, H. (2017). The next ten years of X-ray science. Nature Photonics *11*, 12-14. 10.1038/nphoton.2016.251.
Zhang, Y., Ackels, T., Pacureanu, A., Zdora, M.-C., Bonnin, A., Schaefer, A.T., and Bosch, C. (2022). Sample Preparation and Warping Accuracy for Correlative Multimodal Imaging in the Mouse Olfactory Bulb Using 2-Photon, Synchrotron X-Ray and Volume Electron Microscopy. Frontiers in Cell and Developmental Biology *10*. 10.3389/fcell.2022.880696.
Zimmermann, J., Schalm, T., Sadeghi, M.Z., and Schröder, K.U. (2022). Empirical investigations on the effects of ionizing radiation on epoxy structural adhesives and resins: An overview. International Journal of Adhesion and Adhesives *117*. 10.1016/j.ijadhadh.2021.103014.

Figure 1

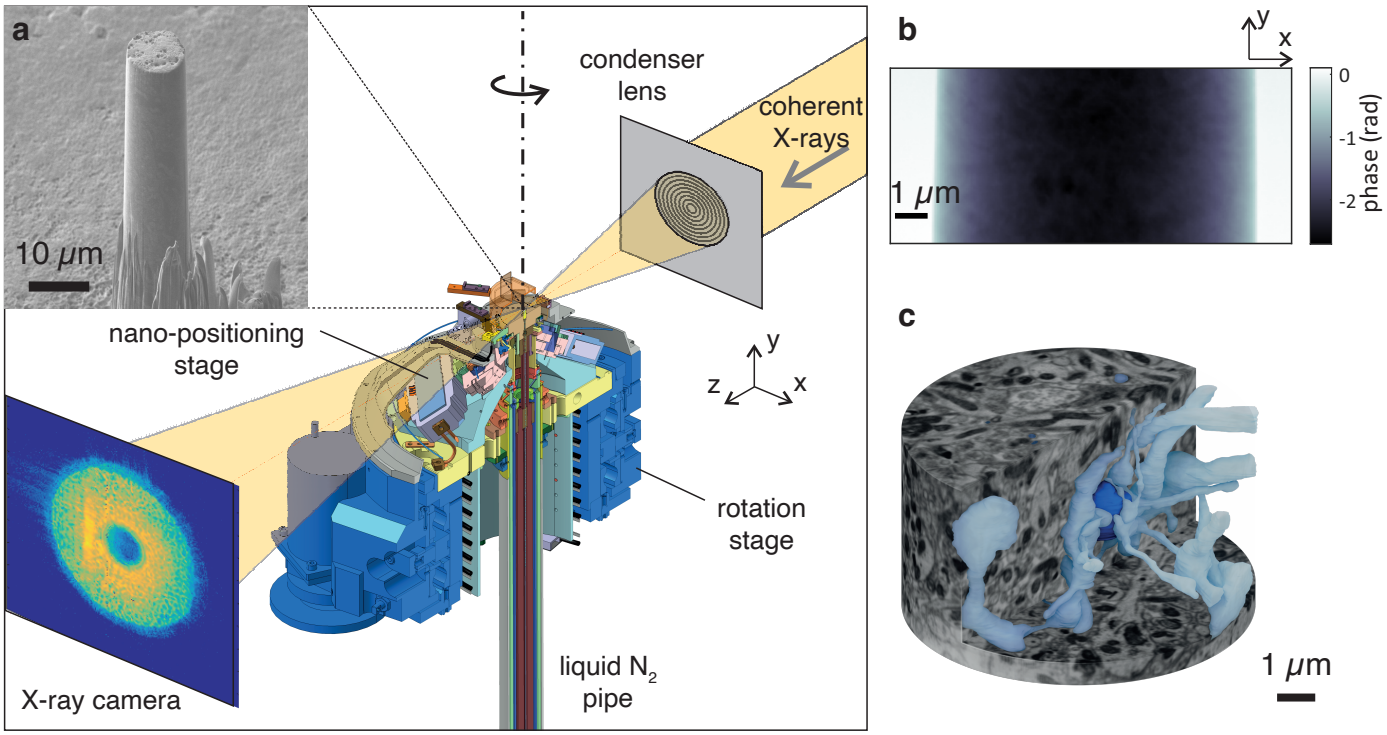
a
10 μm
condenser
lens
coherent
X-rays
nano-positioning
stage
y
z
x
rotation
stage
X-ray camera
liquid N2
pipe
b
y
x
0
-1
-2
phase (rad)
1 μm
c
1 μm

Figure 2

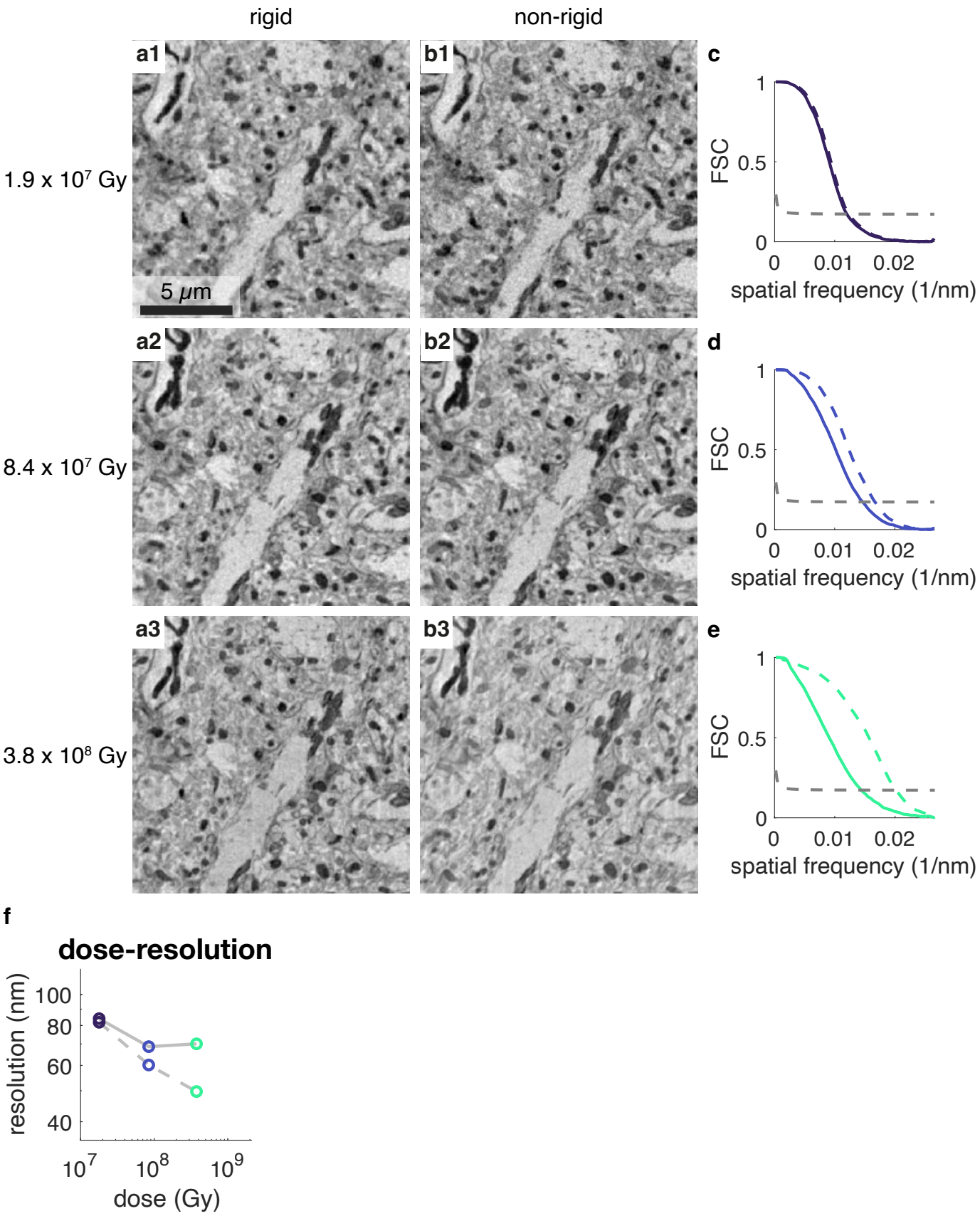
rigid
non-rigid
a1
b1
c
1.9 x 10^7 Gy
5 μm
FSC
1
0.5
0
0
0.01
0.02
spatial frequency (1/nm)
a2
b2
d
8.4 x 10^7 Gy
FSC
1
0.5
0
0
0.01
0.02
spatial frequency (1/nm)
a3
b3
e
3.8 x 10^8 Gy
FSC
1
0.5
0
0
0.01
0.02
spatial frequency (1/nm)
f
dose-resolution
resolution (nm)
100
80
60
40
10^7
10^8
10^9
dose (Gy)

Figure 3

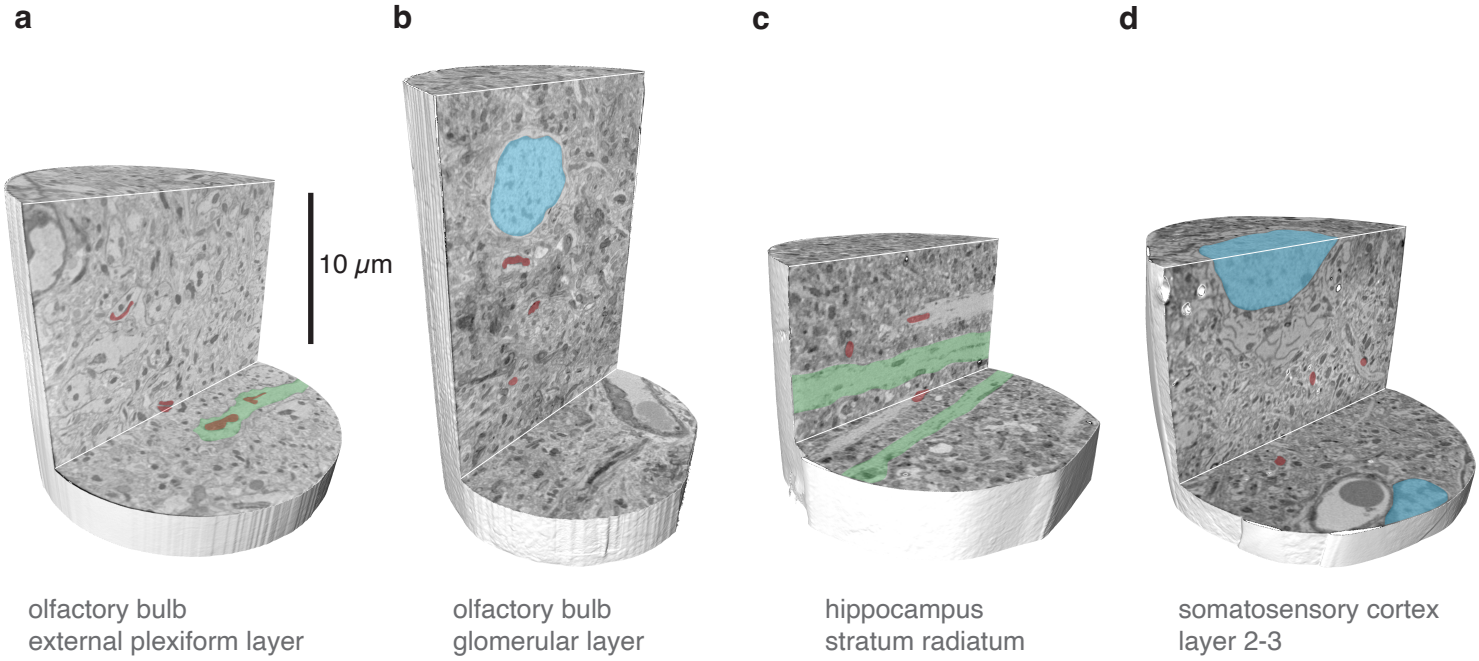
a
b
c
d
10 μm
olfactory bulb
external plexiform layer
olfactory bulb
glomerular layer
hippocampus
stratum radiatum
somatosensory cortex
layer 2-3

Figure 4

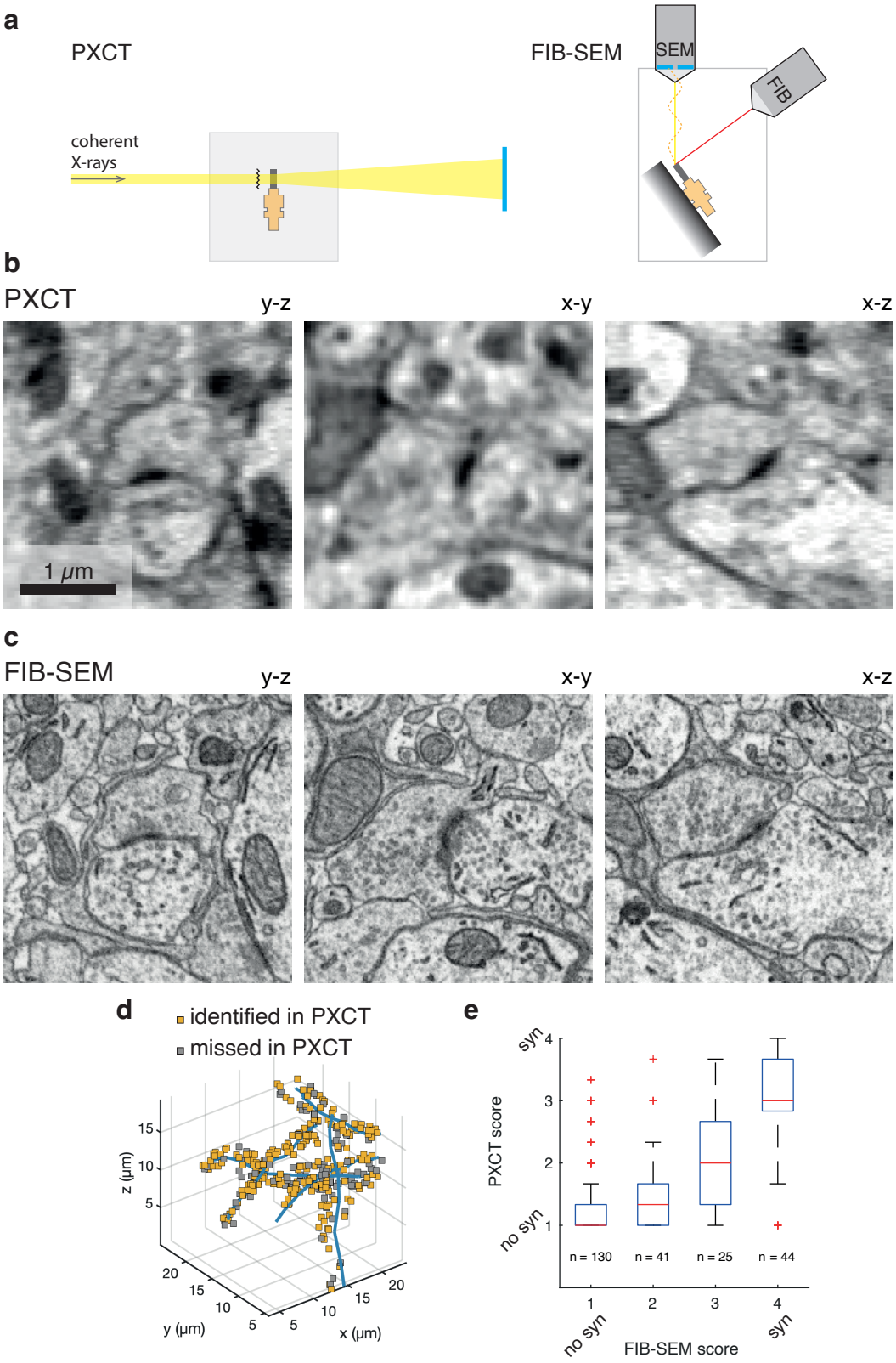
a
PXCT
coherent
X-rays
FIB-SEM
SEM
FIB
b
PXCT
y-z
x-y
x-z
1 μm
c
FIB-SEM
y-z
x-y
x-z
d
identified in PXCT
missed in PXCT
z (μm)
y (μm)
x (μm)
e
PXCT score
FIB-SEM score
no syn
syn
n = 130
n = 41
n = 25
n = 44

Figure 5

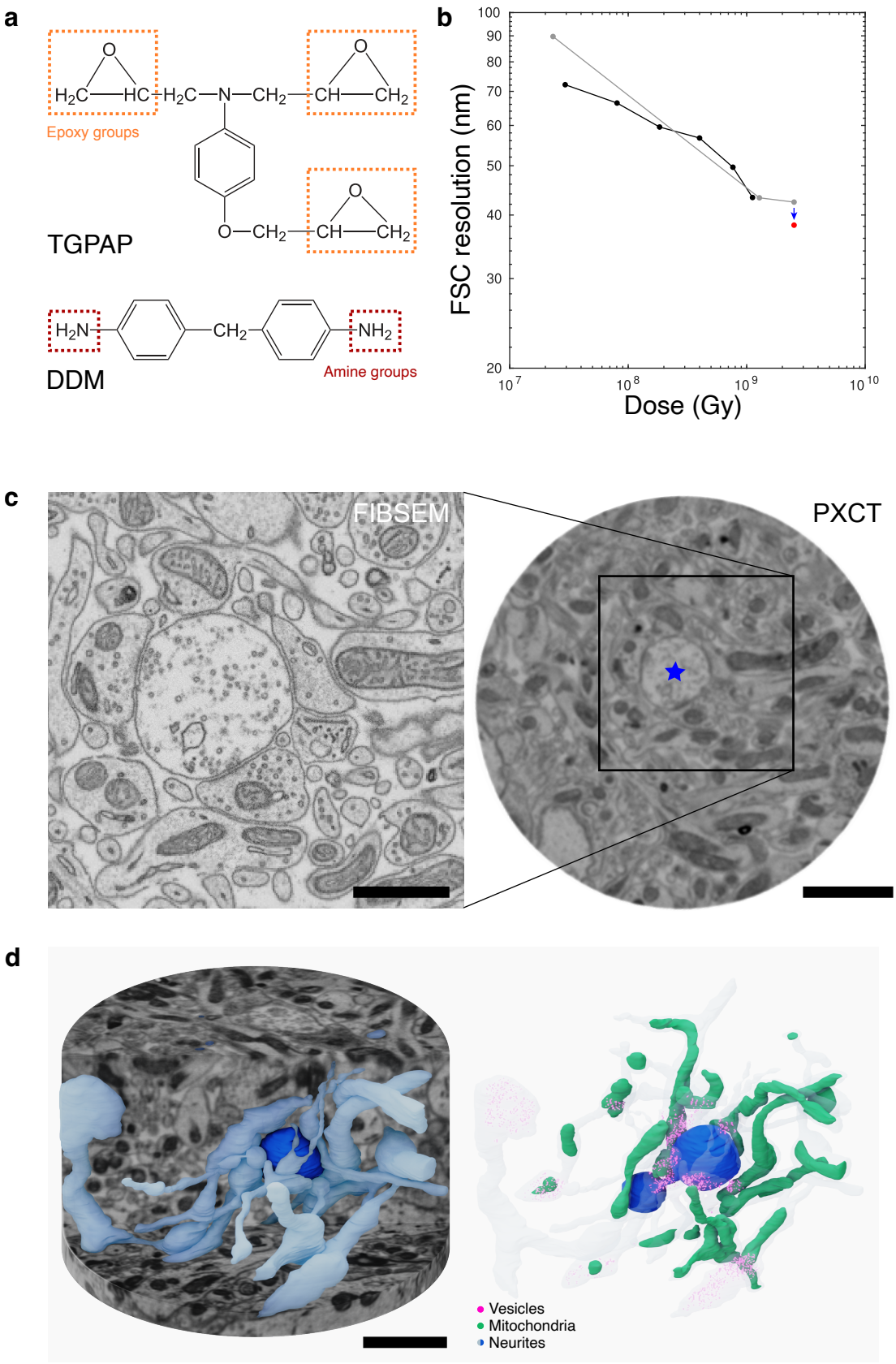
a
Epoxy groups
TGPAP
DDM
Amine groups
b
FSC resolution (nm)
Dose (Gy)
c
FIBSEM
PXCT
d
Vesicles
Mitochondria
Neurites